Kinematic distributions and nuclear effects of J/ψ production in 920 GeV fixed-target proton-nucleus collisions

The HERA-B Collaboration

I. Abt[24], M. Adams[11], M. Agari[14], H. Albrecht[13], A. Aleksandrov[30], V. Amaral[9], A. Amorim[9], S. J. Aplin[13], V. Aushev[17], Y. Bagaturia[13,37], V. Balagura[23], M. Bargiotti[6], O. Barsukova[12], J. Bastos[9], J. Batista[9], C. Bauer[14], Th. S. Bauer[1], A. Belkov[12†], Ar. Belkov[12], I. Belotelov[12], A. Bertin[6], B. Bobchenko[23], M. Böcker[27], A. Bogatyrev[23], G. Bohm[30], M. Bräuer[14], M. Bruinsma[29,1], M. Bruschi[6], P. Buchholz[27], T. Buran[25], J. Carvalho[9], P. Conde[2,13], C. Cruse[11], M. Dam[10], K. M. Danielsen[25], M. Danilov[23], S. De Castro[6], H. Deppe[15], X. Dong[3], H. B. Dreis[15], V. Egorytchev[13], K. Ehret[11], F. Eisele[15], D. Emeliyanov[13], S. Essenov[23], L. Fabbri[6], P. Faccioli[6], M. Feuerstack-Raible[15], J. Flammer[13], B. Fominykh[23†], M. Funcke[11], Ll. Garrido[2], A. Gellrich[30], B. Giacobbe[6], J. Gläß[21], D. Goloubkov[13,34], Y. Golubkov[13,35], A. Golutvin[23], I. Golutvin[12], I. Gorbounov[13,27], A. Gorišek[18], O. Gouchtchine[23], D. C. Goulart[8], S. Gradl[15], W. Gradl[15], F. Grimaldi[6], J. Groth-Jensen[10], Yu. Guilitsky[23,36], J. D. Hansen[10], J. M. Hernández[30], W. Hofmann[14], M. Hohlmann[13], T. Hott[15], W. Hulsbergen[1], U. Husemann[27], O. Igonkina[23], M. Ispiryan[16], T. Jagla[14], C. Jiang[3], H. Kapitza[13,11], S. Karabekyan[26], N. Karpenko[12], S. Keller[27], J. Kessler[15], F. Khasanov[23], Yu. Kiryushin[12], I. Kisel[24], E. Klinkby[10], K. T. Knöpfle[14], H. Kolanoski[5], S. Korpar[22,18], C. Krauss[15], P. Kreuzer[13,20], P. Križan[19,18], D. Krücker[5], S. Kupper[18], T. Kvaratskheliia[23], A. Lanyov[12], K. Lau[16], B. Lewendel[13], T. Lohse[5], B. Lomonosov[13,33], R. Männer[21], R. Mankel[30], S. Masciocchi[13], I. Massa[6], I. Matchikhilian[23], G. Medin[5], M. Medinnis[13], M. Mevius[13], A. Michetti[13], Yu. Mikhailov[23,36], R. Mizuk[23], R. Muresan[10], M. zur Nedden[5], M. Negodaev[13,33], M. Nörenberg[13], S. Nowak[30], M. T. Núñez Pardo de Vera[13], M. Ouchrif[29,1], F. Ould-Saada[25], C. Padilla[13], D. Peralta[2], R. Pernack[26], R. Pestotnik[18], B. AA. Petersen[10], M. Piccinini[6], M. A. Pleier[14], M. Poli[6,32], V. Popov[23], D. Pose[12,15], S. Prystupa[17], V. Pugatch[17], Y. Pylypchenko[25], J. Pyrlik[16], K. Reeves[14], D. Reßing[13], H. Rick[15], I. Riu[13], P. Robmann[31], I. Rostovtseva[23], V. Rybnikov[13], F. Sánchez[14], A. Sbrizzi[1], M. Schmelling[14], B. Schmidt[13], A. Schreiner[30], H. Schröder[26], U. Schwanke[30], A. J. Schwartz[8], A. S. Schwarz[13], B. Schwenninger[11], B. Schwingenheuer[14], F. Sciacca[14], N. Semprini-Cesari[6], S. Shuvalov[23,5], L. Silva[9], L. Sözüer[13], S. Solunin[12], A. Somov[13], S. Somov[13,34], J. Spengler[13], R. Spighi[6], A. Spiridonov[30,23], A. Stanovnik[19,18], M. Starič[18], C. Stegmann[5], H. S. Subramania[16], M. Symalla[13,11], I. Tikhomirov[23], M. Titov[23], I. Tsakov[28], U. Uwer[15], C. van Eldik[13,11], Yu. Vassiliev[17], M. Villa[6], A. Vitale[6,7†], I. Vukotic[5,30], H. Wahlberg[29], A. H. Walenta[27], M. Walter[30], J. J. Wang[4], D. Wegener[11], U. Werthenbach[27], H. Wolters[9], R. Wurth[13], A. Wurz[21], S. Xella-Hansen[10], Yu. Zaitsev[23], M. Zavertyaev[13,14,33], T. Zeuner[13,27], A. Zhelezov[23], Z. Zheng[3], R. Zimmermann[26], T. Živko[18], and A. Zoccoli[6]

[1] NIKHEF, 1009 DB Amsterdam, The Netherlands [a]
[2] Department ECM, Faculty of Physics, University of Barcelona, E-08028 Barcelona, Spain [b]
[3] Institute for High Energy Physics, Beijing 100039, P.R. China
[4] Institute of Engineering Physics, Tsinghua University, Beijing 100084, P.R. China
[5] Institut für Physik, Humboldt-Universität zu Berlin, D-12489 Berlin, Germany [c,d]
[6] Dipartimento di Fisica dell' Università di Bologna and INFN Sezione di Bologna, I-40126 Bologna, Italy
[7] also from Fondazione Giuseppe Occhialini, I-61034 Fossombrone (Pesaro Urbino), Italy
[8] Department of Physics, University of Cincinnati, Cincinnati, Ohio 45221, USA [e]
[9] LIP Coimbra, P-3004-516 Coimbra, Portugal [f]
[10] Niels Bohr Institutet, DK 2100 Copenhagen, Denmark [g]
[11] Institut für Physik, Universität Dortmund, D-44221 Dortmund, Germany [d]
[12] Joint Institute for Nuclear Research Dubna, 141980 Dubna, Moscow region, Russia
[13] DESY, D-22603 Hamburg, Germany
[14] Max-Planck-Institut für Kernphysik, D-69117 Heidelberg, Germany [d]
[15] Physikalisches Institut, Universität Heidelberg, D-69120 Heidelberg, Germany [d]
[16] Department of Physics, University of Houston, Houston, TX 77204, USA [e]
[17] Institute for Nuclear Research, Ukrainian Academy of Science, 03680 Kiev, Ukraine [h]
[18] J. Stefan Institute, 1001 Ljubljana, Slovenia [i]
[19] University of Ljubljana, 1001 Ljubljana, Slovenia
[20] University of California, Los Angeles, CA 90024, USA [j]

2

21 Lehrstuhl für Informatik V, Universität Mannheim, D-68131 Mannheim, Germany
22 University of Maribor, 2000 Maribor, Slovenia
23 Institute of Theoretical and Experimental Physics, 117218 Moscow, Russia [k]
24 Max-Planck-Institut für Physik, Werner-Heisenberg-Institut, D-80805 München, Germany [d]
25 Dept. of Physics, University of Oslo, N-0316 Oslo, Norway [l]
26 Fachbereich Physik, Universität Rostock, D-18051 Rostock, Germany [d]
27 Fachbereich Physik, Universität Siegen, D-57068 Siegen, Germany [d]
28 Institute for Nuclear Research, INRNE-BAS, Sofia, Bulgaria
29 Universiteit Utrecht/NIKHEF, 3584 CB Utrecht, The Netherlands [a]
30 DESY, D-15738 Zeuthen, Germany
31 Physik-Institut, Universität Zürich, CH-8057 Zürich, Switzerland [m]
32 visitor from Dipartimento di Energetica dell' Università di Firenze and INFN Sezione di Bologna, Italy
33 visitor from P.N. Lebedev Physical Institute, 117924 Moscow B-333, Russia
34 visitor from Moscow Physical Engineering Institute, 115409 Moscow, Russia
35 visitor from Moscow State University, 119992 Moscow, Russia
36 visitor from Institute for High Energy Physics, Protvino, Russia
37 visitor from High Energy Physics Institute, 380086 Tbilisi, Georgia

Abstract. Measurements of the kinematic distributions of J/ψ mesons produced in $p-$C, $p-$Ti and $p-$W collisions at $\sqrt{s} = 41.6$ GeV in the Feynman-x region $-0.34 < x_F < 0.14$ and for transverse momentum up to $p_T = 5.4$ GeV/c are presented. The x_F and p_T dependencies of the nuclear suppression parameter, α, are also given. The results are based on $2.4 \cdot 10^5$ J/ψ mesons reconstructed in both the e^+e^- and $\mu^+\mu^-$ decay channels. The data have been collected by the HERA-B experiment at the HERA proton ring of the DESY laboratory. The measurement explores the negative region of x_F for the first time. The average value of α in the measured x_F region is 0.981 ± 0.015. The data suggest that the strong nuclear suppression of J/ψ production previously observed at high x_F turns into an enhancement at negative x_F.

1 Introduction

The DESY experiment HERA-B has measured J/ψ production in proton-carbon, proton-titanium and proton-tungsten collisions at a center-of-mass energy $\sqrt{s} = 41.6\,\mathrm{GeV}$. The results are based on a sample of about $2.4 \cdot 10^5$ inclusively produced J/ψ mesons reconstructed in both dilepton decay channels which includes a fraction of $(6.8\pm0.4)\%$ due to J/ψ's coming from ψ' decays [1] and an additional fraction of $(18.8 \pm 2.8)\%$ from J/ψ's originating from decays of χ_c states [2]. A measurement of the atomic mass number dependence of J/ψ production is derived from a comparison of the different samples. The atomic number dependence of inclusive particle production is often characterized by a power law: $\sigma_{pA} = \sigma_{pN} \cdot A^\alpha$ where σ_{pN} is the proton-nucleon cross section and σ_{pA} is the corresponding proton-nucleus cross section for a target of atomic mass number A. Previous measurements by E866 at Fermilab [3,4] at $\sqrt{s} = 38.8\,\mathrm{GeV}$ and NA50 at CERN [5] at lower energy indicate that $\alpha \sim 0.94 - 0.95$ at $x_F \sim 0$ and decreases to ~ 0.65 as x_F approaches unity [4]. The results presented here provide a first measurement of nuclear effects in charmonium production ex-

tending into the negative part of the Feynman-x spectrum, $-0.34 < x_F < 0.14$ [1].

An understanding of the basic mechanisms responsible for the suppression of charmonium production in proton-nucleus collisions relative to proton-nucleon collisions is a prerequisite for the identification of possible signals of new physics in high-energy heavy-ion data. Interpretations of the existing proton-nucleus data at positive x_F rely on a delicate balance of several processes: nuclear absorption, shadowing of parton densities, energy loss, interactions with co-movers, hadronization of intrinsic $c\bar{c}$ components of the scattering nucleons, and so on. Ad hoc combinations of such elementary mechanisms, considered within various theoretical frameworks [6–8] are able to qualitatively reproduce the observed strong increase of J/ψ suppression as x_F approaches unity [4].

However the presently available data give little guidance in the largely unexplored negative-x_F region where other mechanisms such as formation-time effects can influence the effective nuclear path length of produced states [9–12] and can potentially lead to a decidedly different behavior of α. In contrast to J/ψ production in the positive x_F region, at negative x_F the produced $c\bar{c}$ pair preferentially evolves into a charmonium state before leaving the nucleus and nuclear effects influencing the J/ψ itself become important. Especially in this region, different models and approaches lead to contrasting predictions, for example arising from differing assumptions on energy loss of beam partons or produced $c\bar{c}$ pairs. By extending the current experimental knowledge of the nuclear dependence of J/ψ production towards negative x_F, the measurement described here provides new constraints for possible explanations of the observed nuclear modification pattern. The wide range of transverse momenta (up to $5.4\,\mathrm{GeV}/c$) of the present measurement also permits a complementary measurement of the p_T-broadening effect obtained at lower energies.

The paper is divided into four main sections: an overview of the apparatus, trigger and data samples (Sect. 2), a description of the methods used for the selection and counting of J/ψs (Sect. 3), the measurements of the kinematic distributions (Sect. 4) and the measurements of the nuclear dependence (Sect. 5), followed by concluding remarks (Sect. 6).

2 Apparatus, data taking and Monte Carlo simulation

HERA-B was a fixed-target experiment which studied particles produced in interactions of $920\,\mathrm{GeV}/c$ protons with wire targets positioned in the halo of the HERA beam. The apparatus [13], shown in Fig. 2, was a forward spectrometer with acceptance ranging from 15 to 220 mrad and from 15 to 160 mrad in the bending (xz) and vertical (yz) planes, respectively. Because of this large acceptance

---

[1] A slightly different range is quoted in previous HERA-B publications of J/ψ results due to minor differences in selection cuts.

and the fact that the J/ψ decay tracks were measured before the muon detector (MUON) and the electromagnetic calorimeter (ECAL), HERA-B was the first fixed-target experiment with significant coverage in the region of negative x_F with an accessible range of $x_F \in [-0.34, 0.14]$.

The target system [14] consisted of eight wires which were grouped into two stations separated by 4 cm along the beam line. Each wire could be individually steered in the beam halo by a servo system in order to maintain a constant interaction rate. A total of five wires, differing in shape (round or rectangular), dimensions (between $50\,\mu\mathrm{m}$ and $500\,\mu\mathrm{m}$) and material (C, Ti and W) were used. Depending on running conditions and run-plan, either a single wire or a pair of wires was active for any given data-taking run. The interaction rate was maintained in the range of 2 to 6 MHz, depending on beam conditions and target.

The vertex detector (VDS) [15] comprised eight planar stations of double-sided silicon micro-strip modules, seven of which were mounted in Roman pots built into the vacuum vessel and operated at a minimum distance of 10 mm from the beam. A track traversed typically three stations, yielding twelve measurement points in four stereo views. Vertex resolutions of 450 and $50\,\mu\mathrm{m}$ in the beam direction and in the transverse plane, respectively, were achieved. The eighth station was on a fixed mount immediately following the exit window of the main vertex system, 2 m downstream from the target.

The momenta of charged tracks were measured from their bending through a vertical magnetic field of integral 2.13 Tm. The main tracker was located between 2 to 13 m downstream of the target, with one station preceding the magnet, four stations immediately after the magnet (Pattern Chambers, PCs) and another two (Trigger Chambers, TCs) after the Ring Imaging Cherenkov detector (RICH). Each station contained an inner part [16] (made of micro-strip gas chambers and covering angles less than 20 mrad) which was not included in the trigger system and therefore does not play a role in the analysis presented here. The outer part (OTR) [17] was composed of honeycomb drift chambers, with wire pitches of 5 mm closer to the beam pipe and 10 mm elsewhere. The final momentum resolution for muons was found to be $\sigma_p/p[\%] = (1.61 \pm 0.02) + (0.0051 \pm 0.0006) \cdot p\,[\mathrm{GeV}/c]$ [17].

The identification of the J/ψ in its dilepton decay modes as well as the first stage of the trigger system relied mainly on the signals provided by the ECAL [19] and MUON [20] systems. The ECAL was a sampling calorimeter using shashlik technology with Pb and W absorbers sandwiched between scintillator layers. It was divided into three sections (Inner, Middle and Outer) with cell widths of 2.2, 5.5 and 11 cm, respectively, to roughly equalize occupancies. The inner section used W absorbers, while the middle and outer sections used Pb. The design was optimized for good electron/photon energy resolution and for electron-hadron discrimination. The final energy resolution reached by the detector can be written in the form $\sigma_E/E = A/\sqrt{E} \oplus B$ (E measured in GeV), with $A = 0.206$, 0.118 and 0.108 and $B = 0.012$, 0.014 and
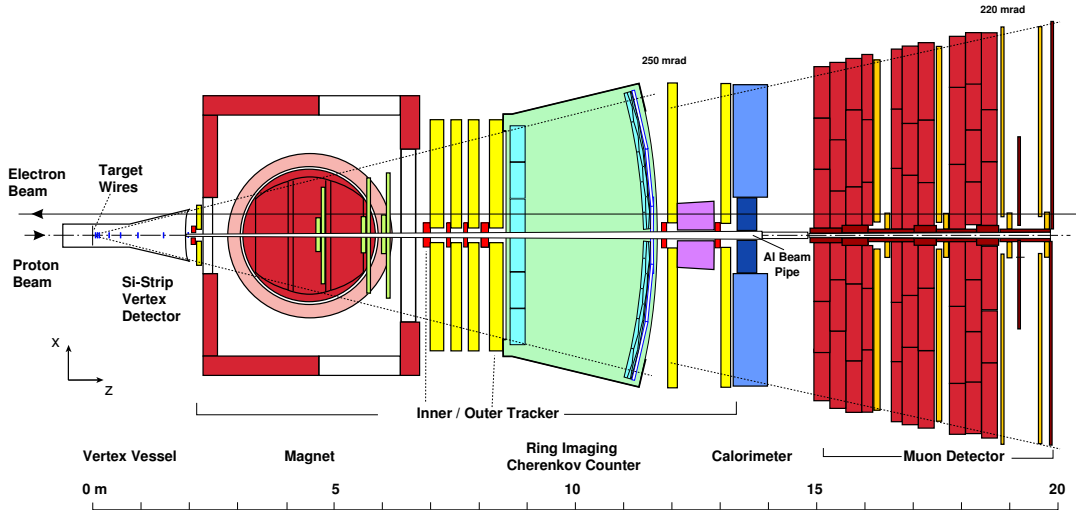
Fig. 1. Top view of the HERA-B detector.

0.014, for the Inner, Middle and Outer sections, respectively. The spatial resolution ranged from 1 to 10 mm depending on the calorimeter section and on the energy of the particle [19].

The MUON system consisted of four tracking stations interleaved with iron or concrete absorbers. As in the main tracker, two different technologies were used: gas pixel chambers in the innermost region and conventional tube chambers in the outer part. For the last two stations, not only the anode wires of the tubes but also the segmented cathodes were read out. Signals from the cathode pads were also given as inputs to the trigger.

The RICH [18] detector relied on a C_4F_{10} radiator and was used extensively in other analyses for $\pi/K/p$ separation. It also played a small role in the present analysis as a means to reject backgrounds in the dilepton analysis, particularly from kaon decays.

The trigger system selected both e^+e^- and $\mu^+\mu^-$ signatures and was organized into three levels: a pretrigger [19,21], a First Level Trigger (FLT [22]) and a software-based Second Level Trigger (SLT [23]). The pretrigger used signals from the ECAL and MUON detectors and required the presence of at least two reconstructed ECAL clusters with transverse energy above 1.1 GeV or the presence of two muon candidates, defined as coincidences of projective pads in the last two MUON layers. Starting from pretrigger seeds, the FLT attempted to find tracks in a subset of the OTR tracking layers and required that at least one of the seeds resulted in a reconstructed track. Starting again from the pretrigger seeds, the SLT searched for tracks inside regions-of-interest generated by the pretriggers using all OTR layers and continued the tracking through the VDS. Finally, at least two fully reconstructed tracks consistent with the hypothesis of a common vertex were required. Events passing the SLT were transferred to a computer farm which provided full online reconstruction of a fraction of the events for data quality monitoring. The global trigger suppression factor, 5×10^4, resulted in an event archival rate of about 100 Hz.

A total of 160 million dilepton triggered events were recorded between October 2002 and February 2003, together with an approximately fixed 10 Hz rate of minimum bias events which were used for monitoring and luminosity determination. The event samples were distributed between three target materials: carbon (64%), tungsten (32%) and a small fraction with titanium (4%).

A full Monte Carlo (MC) simulation is used to determine the triggering (except for FLT, see below), reconstruction and selection efficiencies. In view of the range of physics topics addressed by the experiment (pA inelastic interactions, meson decays and heavy flavor physics), the MC generator is built as a combination of two standard tools: PYTHIA 5.7 [24] for heavy flavor (b or c) quark production in pN interactions and subsequent hadronization and FRITIOF 7.02 [25] for light quark production, secondary interactions in detector materials and generic pA inelastic interactions. The production of the J/ψ is simulated by first generating the basic hard process $pN \rightarrow c\bar{c}X$ and subsequent $c\bar{c}$ hadronization with PYTHIA and then giving the remaining energy and momentum (X) of the interaction to FRITIOF for generation of further interactions inside the hit nucleus. The generated particles are then given as input to the GEANT 3.21 based package [26] for full simulation of active (instrumented) and inactive (support structure) elements of the detector and for the digitization of the electronic signals.

To describe the kinematic characteristics of the produced J/ψs as accurately as possible, an x_F, p_T, and decay-angle dependent weight is assigned to each event and used in the subsequent analysis to force the simulated J/ψ production and decay distributions to agree with the corresponding measured distributions for each target material. The weights are determined by an iterative procedure in which computed corrections are based on comparisons of MC event distributions after reconstruction and selection cuts with the corresponding distributions from data.

The FLT efficiency is derived from an efficiency map which is determined from the data itself. Since the SLT result is completely independent of the FLT, and since the FLT triggered on only one of the two lepton tracks, the efficiency map can be determined by checking the presence of the second J/ψ lepton on the FLT. Using the efficiency map, each event is assigned a weight which multiplies the kinematic weight discussed above.

To accurately reproduce the actual working configuration at the time of data-taking and properly account for time variations of working conditions, the full data taking period is divided into five calibration periods of similar lengths, each matched by a corresponding simulation sample for which the efficiencies of the individual detector cells are evaluated and given as input to the MC. The MC samples are reconstructed and analyzed with the same methods and software packages used for the analysis of the real data.

3 J/ψ selection and counting

The electron and muon candidates are selected with common track- and vertex-selection criteria while channel-specific methods are applied for lepton identification and the treatment of the J/ψ signal.

All tracks passing the SLT are initially considered as lepton candidates. The track reconstruction procedure consists of finding straight segments in the VDS and PCs independently, matching them to each other and also to segments in the TCs. A full, iterative fit of found tracks is then performed. To reject incorrectly reconstructed or ghost tracks, loose cuts on the minimum number of hits in the VDS and OTR, as well as on the χ^2 probability of the track fit are applied by the event reconstruction algorithms. The detector acceptance and trigger requirements effectively limit the momentum and transverse momentum ranges of lepton tracks to $5 < p < 200\,\mathrm{GeV}/c$ and $0.7 < p_T < 5.0\,\mathrm{GeV}/c$, respectively. For each event, among all possible pairs of oppositely charged lepton candidates consistent with a common vertex (χ^2 probability greater than 1%), only the pair with the best particle identification (see below) for both leptons is accepted.

3.1 Dimuon channel

Since muons are the only particles having a significant probability of penetrating through the absorbers of the MUON detector, only minimal selection cuts are needed to obtain a clean sample (see also [1]). The background of muons from pion and kaon decays is reduced by imposing tighter cuts on the quality of the track fit and on the matching of track segments in the VDS, OTR and MUON. Doing so rejects the typical "broken trajectories" produced by decays into leptons. Contamination from kaons is further reduced by discarding tracks with high values of the corresponding RICH likelihood. After all selection cuts, the background under the J/ψ signal is reduced by
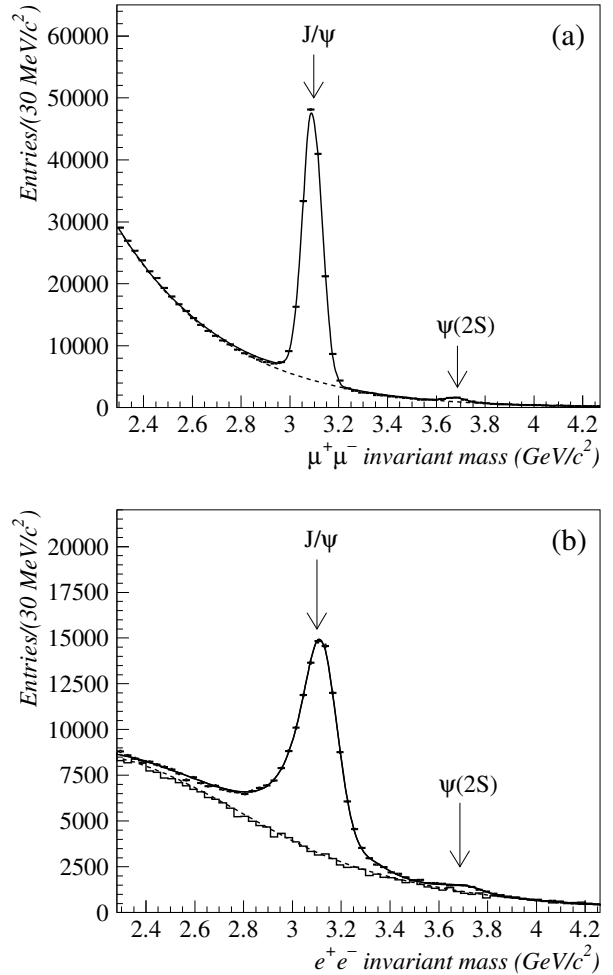

Fig. 2. The $\mu^+\mu^-$ (a) and e^+e^- (b) invariant mass distributions for the full data sample in the J/ψ mass region. The continuous lines represent the result of fits performed with the functions described in the text; the dashed lines are the fitted backgrounds. The histogram in (b) represents the background shape as determined from combinations of tracks reconstructed in different events.

a factor of 2.5 with respect to the triggered data with a loss of about 11% of the signal.

Fig. 2(a) shows the resulting dimuon mass spectrum together with the result of a fit to a sum of three functions [27], which model the J/ψ and $\psi(2S)$ signals and the exponential background. The J/ψ and $\psi(2S)$ signals are each modeled as a superposition of three Gaussians with a common mean which takes into account track resolution and effects of Molière scattering and a function representing the radiative tail due to the decay $J/\psi \to \mu^+\mu^-\gamma$. The background is described by an exponential of a second-order polynomial. The fitted position and width of the J/ψ peak are $3.0930 \pm 0.0002\,\mathrm{GeV}/c^2$ and $40 \pm 1\,\mathrm{MeV}/c^2$, respectively.
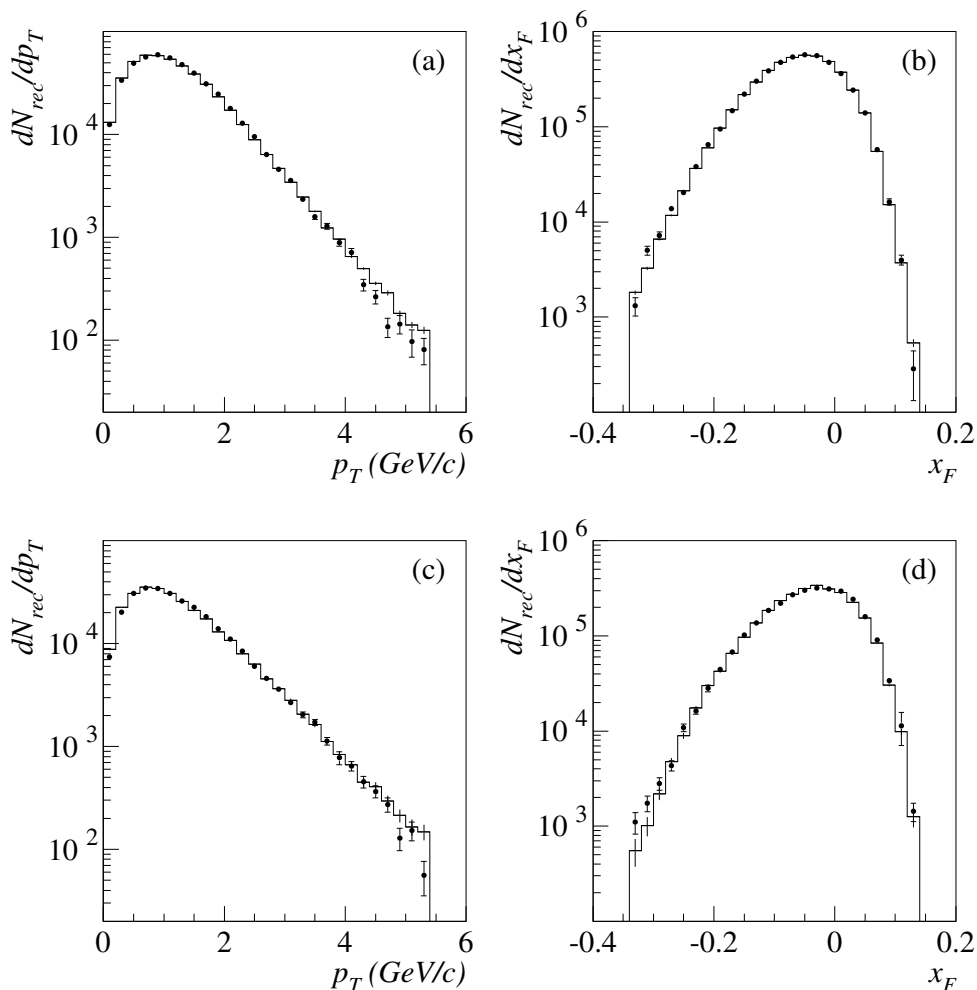
Fig. 3. Distribution of the number of J/ψs reconstructed in the carbon target sample (points) and in the corresponding MC data (histograms, arbitrarily re-normalized) as a function of p_T and x_F. (a) and (b): muon channel, (c) and (d): electron channel.

Table 1. The numbers of reconstructed J/ψs after all selection cuts in the dimuon and dielectron channels, and for different target materials.

Channel	C	Ti	W	Total
$\mu^+\mu^-$	94800	8060	48100	152000
e^+e^-	57700	4280	25300	87200

3.2 Dielectron channel

The J/ψ selection in the dielectron channel is affected by major background contributions from charged hadrons which produce energetic ECAL clusters and by overlapping photon and charged-hadron energy deposits in the ECAL. For this reason, the electron identification requirements were the subject of careful optimization studies which resulted in much more stringent selection cuts than for the muon sample.

A cut on the transverse energy of the ECAL cluster ($E_T > 1.15$ GeV) is applied in order to mask different threshold cuts applied at the pretrigger level for the various acquisition periods.

The reconstructed momentum vectors of electrons and positrons are corrected for energy loss from bremsstrahlung (BR) emission in the materials in front of the magnet. For each electron track, an attempt to identify an ECAL cluster due to a BR photon is made by looking for an energy deposition in coincidence with the extrapolation of the associated VDS track segment to the ECAL. Any recovered energy (about 18% of the initial electron energy on average) is then added to the momentum measured by the tracking system. Since BR is a clear signature for an electron track, it is also exploited to obtain substantial background reduction which is essential for accurate J/ψ counting. The baseline results of the analysis are obtained by requiring that at least one lepton of a decaying J/ψ has an associated BR cluster. This requirement reduces the signal by about 30% and suppresses the background by more than a factor of two. Alternative requirements (no

BR requirement, only one, or both electrons emitting BR) lead to very different background shapes and amounts. The differences are exploited for systematic studies on the stability of signal counting and on the correctness of the MC simulation.

Adjustments to the measured momenta of electron tracks were applied to compensate for differences in multiple scattering between electrons and muons since the track-fitter had been calibrated for muons. For this purpose, a correction map, determined from the shift of the J/ψ peak position in different kinematic regions was used.

Additional selection cuts are applied to further improve the significance of the dielectron signal. A particularly discriminating variable is the ratio E/p, where E is the energy of an ECAL cluster and p is the momentum of the associated track. The E/p distribution for electrons has a Gaussian shape with a mean value close to 1 and width varying between 6.4% and 7.4% depending on calorimeter sector. Values of E/p much lower than 1 are mainly due to particles, mostly hadrons, which release only part of their energy in the calorimeter. Further selection variables used in the analysis are the distances Δx and Δy – along the x and y directions – between the reconstructed cluster and the track position extrapolated to the ECAL. The Δx and Δy distributions for electrons are, apart from a small tail, well described by Gaussians centered at zero with widths between 0.2 and 1.0 cm depending on calorimeter sector. Cuts on these quantities lead to a significant reduction of the contamination from hadrons and random cluster-track matches which are characterized by significantly wider distributions. The selection of the candidate electron-positron pairs is further refined by putting an upper bound on the distance of closest approach (Δb) between the two accepted tracks near the vertex.

All the requirements described above have been simultaneously optimized by maximizing the significance $S/\sqrt{S+B}$ of the J/ψ signal (S) – taken from the MC (scaled to the number of J/ψ in the data) – with respect to the background (B) – evaluated from the data. The optimal ranges for the different cut variables depend on the number (one or two) of BR clusters associated to the electron-positron pair. When both electron and positron have a BR cluster correlated to the track, where the cluster position was determined by hierarchical clustering [19], the event is already rather cleanly reconstructed and only one additional request (for each lepton candidate), $(E/p - 1)/\sigma_{E/p} > -3.6$, is applied. When only one of the two possible BR clusters is found, the accepted ranges are determined for each lepton as $-3.6 < (E/p - 1)/\sigma_{E/p} < 5.4$, $|\Delta x|/\sigma_{\Delta x} < 7.0$, $|\Delta y|/\sigma_{\Delta y} < 3.3$ and $\Delta b < 370\,\mu$m, respectively.

The combined selection cuts increase the S/B ratio of the J/ψ by about a factor of 10 with respect to triggered events, and have an overal efficiency of $(45 \pm 4)\%$ as evaluated using the data and verified with the simulation – the rather large uncertainty is due to the difficulty of counting the signal when no cuts are applied. As can be seen in Fig. 2(b), the significance of the optimized J/ψ signal

after momentum correction and selection cuts, although less than that of the muon channel shown in Fig. 2(a), is nonetheless such that the electron sample significantly enhances the statistical precision of the final results. The method adopted for counting the signal, derived from a study of the signal shape in MC, uses a Gaussian shape for the right part of the peak and a Breit-Wigner shape for the left part to account for the sizable asymmetry of the signal caused by missing BR energy and the contribution of the radiative decay $J/\psi \rightarrow e^+e^-\gamma$. The background is parametrized with a Gaussian at lower mass values and an exponential at higher mass, joined together such that the resulting curve is smooth, where the transition point is outside the Gaussian peak. The position and width of the J/ψ peak (Gaussian Part) as determined from the fit are 3.110 ± 0.001 GeV/c^2 and 72 ± 1 MeV/c^2, respectively.

The yields of selected J/ψ candidates for the two decay channels and for each target material are listed in Table 1. Fig. 3 shows (for the carbon data) a comparison between data and MC of the distributions of reconstructed J/ψs as a function of the kinematic variables p_T and x_F.

4 Kinematic distributions

4.1 Results

The present analysis adopts the degrees of freedom p_T, x_F and Φ (azimuthal production angle) for the description of the J/ψ production kinematics. Single-variable distributions are obtained according to the formula (here written e.g. for x_F)

$$\frac{dN_{J/\psi}}{dx_F}(x_F) = \frac{\Delta N_{J/\psi}^{\text{rec}}(x_F)}{\epsilon_{J/\psi}(x_F)\,\Delta x_F}, \qquad (1)$$

where $\Delta N_{J/\psi}^{\text{rec}}(x_F)$ is the fraction of J/ψs reconstructed in a given x_F interval of width Δx_F and $\epsilon_{J/\psi}(x_F)$ is the global (trigger, reconstruction and selection) efficiency for that interval integrated over all other kinematic variables (including the J/ψ decay degrees of freedom) using the tuned MC. In each case, the signal is also integrated over all other kinematic variables. All distributions are normalized to unit area[2]. The average resolutions for the variables p_T, x_F and Φ are, respectively, 0.065 GeV/c, 0.0024 and 3.3°, much smaller than the chosen bin widths of 0.2 GeV/c, 0.02 and 18°.

The final p_T and x_F distributions for the three materials, are shown in Figs. 4 and 5. The error bars include statistical and systematic uncertainties added in quadrature. The corresponding numbers can be found in Tables 2 and 3. The final distributions and systematic uncertainties are evaluated by fixing the input parameters and assumptions of the analysis to a variety of values within

---

[2] The absolute J/ψ yield in proton-nucleus collisions at 920 GeV/c was the subject of a measurement performed using minimum bias data [28].

Table 2. J/ψ p_T distributions (dN/dp_T, normalized to their integrals over the measured range) for three target materials with statistical and systematic uncertainties.

p_T (GeV/c) min	max	C ($\times 10^{-2}$)			Ti ($\times 10^{-2}$)			W ($\times 10^{-2}$)		
0.0	0.2	10.74	± 0.28	± 0.72	8.5	± 0.9	± 1.9	8.5	± 0.3	± 1.1
0.2	0.4	30.94	± 0.46	± 0.69	26.3	± 1.7	± 2.0	25.1	± 0.7	± 1.1
0.4	0.6	47.36	± 0.61	± 0.66	40.4	± 2.1	± 2.1	39.9	± 0.7	± 1.1
0.6	0.8	55.90	± 0.73	± 0.62	54.8	± 2.3	± 2.1	51.9	± 0.9	± 1.1
0.8	1.0	61.10	± 0.66	± 0.58	57.6	± 2.3	± 2.1	56.5	± 1.0	± 1.1
1.0	1.2	58.16	± 0.70	± 0.53	52.3	± 2.1	± 2.0	53.8	± 1.0	± 1.0
1.2	1.4	51.11	± 0.66	± 0.49	51.5	± 2.2	± 1.9	52.8	± 1.0	± 1.0
1.4	1.6	43.57	± 0.62	± 0.44	44.2	± 1.9	± 1.8	44.58	± 0.85	± 0.87
1.6	1.8	34.84	± 0.58	± 0.40	37.1	± 2.0	± 1.6	37.89	± 0.76	± 0.77
1.8	2.0	28.17	± 0.53	± 0.35	27.9	± 1.5	± 1.4	29.46	± 0.66	± 0.68
2.0	2.2	20.78	± 0.42	± 0.31	22.0	± 1.4	± 1.3	23.02	± 0.66	± 0.58
2.2	2.4	15.37	± 0.33	± 0.27	16.0	± 1.2	± 1.1	17.81	± 0.52	± 0.49
2.4	2.6	11.18	± 0.26	± 0.23	11.4	± 1.0	± 0.9	13.06	± 0.44	± 0.40
2.6	2.8	7.73	± 0.23	± 0.20	6.89	± 0.72	± 0.71	9.56	± 0.37	± 0.33
2.8	3.0	5.59	± 0.20	± 0.17	4.99	± 0.57	± 0.57	7.45	± 0.36	± 0.26
3.0	3.2	4.22	± 0.16	± 0.14	3.80	± 0.50	± 0.44	4.68	± 0.24	± 0.20
3.2	3.4	2.79	± 0.12	± 0.12	3.18	± 0.56	± 0.33	3.77	± 0.25	± 0.15
3.4	3.6	1.90	± 0.10	± 0.09	1.96	± 0.34	± 0.25	2.75	± 0.18	± 0.11
3.6	3.8	1.402	± 0.082	± 0.077	1.30	± 0.25	± 0.18	2.16	± 0.15	± 0.08
3.8	4.0	0.879	± 0.064	± 0.062	0.92	± 0.25	± 0.13	1.27	± 0.11	± 0.06
4.0	4.2	0.672	± 0.051	± 0.049	0.65	± 0.23	± 0.09	0.746	± 0.081	± 0.042
4.2	4.4	0.338	± 0.036	± 0.039				0.542	± 0.067	± 0.029
4.4	4.6	0.257	± 0.030	± 0.030				0.383	± 0.056	± 0.019
4.6	4.8	0.153	± 0.025	± 0.023				0.263	± 0.049	± 0.013
4.8	5.0	0.134	± 0.023	± 0.018				0.212	± 0.041	± 0.008
5.0	5.2	0.130	± 0.028	± 0.013				0.115	± 0.036	± 0.005
5.2	5.4	0.042	± 0.011	± 0.010				0.061	± 0.022	± 0.003

their range of uncertainties (see list below) and carrying through the full analysis. The kinematic distributions are finally obtained by averaging over decay channels for each set of input parameters and assumptions. The central value for each bin is the mid-point of the distribution of values thus obtained and the systematic uncertainty is the maximum spread of the obtained values divided by $\sqrt{12}$. The stability tests are described in the following list.

– The impact of *selection and optimization* requirements is evaluated by changing the cuts on momentum and transverse momentum of muon and electron candidates with respect to the intrinsic thresholds of the trigger selection, and by scanning systematically the values of all cut variables used for the optimization of the dimuon and dielectron signals (including, for the latter, different BR requirements).

– The uncertainty associated to the *signal counting method* has been estimated from the variation of the results obtained with the adoption of modified background and signal functions. Special attention is given to the background evaluation of the dielectron channel: as an alternative to the fit with an assumed background function, a background shape constructed by mixing real events (combining each track with one of opposite-charge from a different event, see Fig. 2(b))

has been used in an unbinned maximum-likelihood fit of the invariant mass spectrum. A further cross-check is represented by the comparison between the efficiency-corrected J/ψ yield obtained with different BR requirements (and therefore different background shapes). When the BR requirement is removed, the evaluation of the number of J/ψs becomes less stable due to increased background, but the variation of the efficiency-corrected yield with respect to the standard selection is estimated to be lower than 5%.

– The systematic uncertainties also account for the stability of the results when specific *acquisition periods and conditions* are selected. A large subsample of the collected events was produced on two target wires of different materials operated simultaneously. The comparison of these data with those acquired with a single target provides an indication of the extent to which the measurements are affected by variations of the experimental conditions.

– The results are sensitive to the shape of the J/ψ *decay angular distribution* assumed in the MC generator. The hypothesis – made by previous experiments – that the J/ψ is produced in an unpolarized state is not supported by the HERA-B data [29]. There is, moreover, an indication that the polarization increases in magnitude with decreasing p_T, while no significant x_F depen-

Table 3. J/ψ x_F distributions (dN/dx_F, normalized to their integrals over the measured range) for the three target materials with statistical and systematic uncertainties.

x_F min	max	C	Ti	W
-0.34	-0.32	$0.221 \pm 0.045 \pm 0.035$		$0.228 \pm 0.061 \pm 0.058$
-0.32	-0.30	$0.412 \pm 0.044 \pm 0.039$		$0.372 \pm 0.070 \pm 0.059$
-0.30	-0.28	$0.429 \pm 0.037 \pm 0.044$		$0.431 \pm 0.076 \pm 0.061$
-0.28	-0.26	$0.492 \pm 0.031 \pm 0.049$		$0.593 \pm 0.065 \pm 0.062$
-0.26	-0.24	$0.639 \pm 0.036 \pm 0.054$	$0.88 \pm 0.16 \pm 0.05$	$0.812 \pm 0.065 \pm 0.063$
-0.24	-0.22	$0.798 \pm 0.035 \pm 0.058$	$0.90 \pm 0.13 \pm 0.05$	$0.846 \pm 0.057 \pm 0.065$
-0.22	-0.20	$1.067 \pm 0.036 \pm 0.063$	$1.41 \pm 0.15 \pm 0.06$	$1.393 \pm 0.066 \pm 0.066$
-0.20	-0.18	$1.247 \pm 0.034 \pm 0.068$	$1.53 \pm 0.15 \pm 0.06$	$1.361 \pm 0.059 \pm 0.068$
-0.18	-0.16	$1.504 \pm 0.035 \pm 0.073$	$1.88 \pm 0.14 \pm 0.07$	$1.725 \pm 0.057 \pm 0.069$
-0.16	-0.14	$1.791 \pm 0.030 \pm 0.078$	$1.87 \pm 0.12 \pm 0.07$	$2.000 \pm 0.063 \pm 0.070$
-0.14	-0.12	$2.119 \pm 0.033 \pm 0.082$	$2.21 \pm 0.14 \pm 0.08$	$2.171 \pm 0.065 \pm 0.072$
-0.12	-0.10	$2.374 \pm 0.031 \pm 0.087$	$2.61 \pm 0.13 \pm 0.08$	$2.477 \pm 0.056 \pm 0.073$
-0.10	-0.08	$2.710 \pm 0.033 \pm 0.092$	$2.71 \pm 0.13 \pm 0.09$	$2.713 \pm 0.056 \pm 0.074$
-0.08	-0.06	$3.074 \pm 0.039 \pm 0.097$	$3.04 \pm 0.13 \pm 0.09$	$3.022 \pm 0.051 \pm 0.076$
-0.06	-0.04	$3.33 \pm 0.05 \pm 0.10$	$3.45 \pm 0.14 \pm 0.10$	$3.161 \pm 0.052 \pm 0.077$
-0.04	-0.02	$3.51 \pm 0.04 \pm 0.11$	$3.73 \pm 0.15 \pm 0.10$	$3.318 \pm 0.055 \pm 0.078$
-0.02	0.00	$3.56 \pm 0.04 \pm 0.11$	$3.78 \pm 0.16 \pm 0.11$	$3.413 \pm 0.057 \pm 0.080$
0.00	0.02	$3.54 \pm 0.05 \pm 0.12$	$3.56 \pm 0.18 \pm 0.11$	$3.349 \pm 0.065 \pm 0.081$
0.02	0.04	$3.47 \pm 0.05 \pm 0.12$	$3.68 \pm 0.22 \pm 0.12$	$3.207 \pm 0.071 \pm 0.082$
0.04	0.06	$3.18 \pm 0.07 \pm 0.13$	$3.80 \pm 0.30 \pm 0.12$	$2.998 \pm 0.093 \pm 0.084$
0.06	0.08	$2.97 \pm 0.08 \pm 0.13$	$3.40 \pm 0.33 \pm 0.13$	$2.67 \pm 0.11 \pm 0.09$
0.08	0.10	$2.90 \pm 0.14 \pm 0.13$	$1.65 \pm 0.33 \pm 0.13$	$2.60 \pm 0.17 \pm 0.09$
0.10	0.12	$2.33 \pm 0.28 \pm 0.14$	$2.44 \pm 0.93 \pm 0.14$	$2.21 \pm 0.28 \pm 0.09$
0.12	0.14	$1.54 \pm 0.45 \pm 0.14$		$1.80 \pm 0.65 \pm 0.09$

dence is found. Since a longitudinally polarized J/ψ is detected more efficiently due to the lower probability that its decay leptons escape detection by passing through the uninstrumented region near the beam, the kinematic dependence of the polarization assumed in the MC influences the shape of the efficiency-corrected p_T and/or x_F spectra. The systematic stability tests therefore include a variety of different assumptions for polarization (including longitudinal, p_T-dependent polarization – also considering the possibility of an A-dependent polarization – and the absence of polarization).

The distribution of the azimuthal production angle Φ has been evaluated as a systematic check of the uniformity of the MC description of the geometrical acceptance. Fig. 6 shows the result obtained when combining the full data reconstructed in both decay channels: the points are consistent, within the statistical uncertainties, with the expected flat distribution.

The dimuon and dielectron results (which, as discussed below, are found to be compatible) are averaged such that correlations in their systematic uncertainties are taken into account. Such correlations have been estimated by maintaining (when possible) a parallelism among the two channels when evaluating the effect of each single systematic test. The assumed polarization hypothesis is found to be the dominating source of uncertainty in the final results – especially for the lower part of the p_T distribution – as

well as the most important cause of correlation between the two analyses. Relative to this uncertainty, the signal selection cuts are in general responsible for negligible systematic variations, except for the most positive part of the x_F spectrum, where acceptance corrections increase dramatically due to the low-angle detector acceptance cut-off near the beam.

The results are well represented – and can therefore be described – by the following interpolating functions which are further motivated in the following section:

$$\frac{dN}{dp_T} \propto p_T \left(1 + \frac{1}{\beta - 2} \frac{p_T^2}{\langle p_T^2 \rangle} \right)^{-\beta}, \qquad (2)$$

$$\frac{dN}{dx_F} \propto \exp \left[-\ln 2 \left| \frac{x_F - \Delta x_F}{w_{x_F}} \right|^\gamma \right]. \qquad (3)$$

The parameters $\langle p_T^2 \rangle$, β, w_{x_F} (width at half maximum), Δx_F (shift of the center of the distribution with respect to $x_F = 0$) and γ are left free in the fit of the distributions. The resulting values are listed in Table 4 for each target material. The systematic uncertainties of the parameters have been determined from the maximum variation (divided by $\sqrt{12}$) of the results obtained by re-fitting the distributions after each of the stability tests described above. The normalized χ^2 obtained from the fits of the combined dimuon-dielectron results are, respectively, 1.5, 0.8 and 2.1 for the p_T distributions of carbon, titanium and tungsten, and 1.1, 1.5 and 1.2 for the three x_F distri-

Table 4. Parameter values obtained from the fit of the kinematic distributions of each of the three target samples to the functions described in the text (Eqs. 2 and 3). The first of the given uncertainty ranges is statistical and the second is systematic. Significant parameter correlations are found between w_{x_F} and $|\Delta x_F|$ (-70%) and between w_{x_F} and γ ($+70\%$). The parameters of the p_T distribution are practically uncorrelated due to the choice of the fitting function.

Channel	Param.	C			Ti			W		
$\mu^+\mu^-$	$\langle p_T^2 \rangle$	2.141	$\pm$ 0.011	$\pm$ 0.014	2.200	$\pm$ 0.044	$\pm$ 0.015	2.435	$\pm$ 0.017	$\pm$ 0.026
	β	7.31	$\pm$ 0.20	$\pm$ 0.14	9.3	$\pm$ 1.6	$\pm$ 0.5	8.09	$\pm$ 0.34	$\pm$ 0.24
e^+e^-	$\langle p_T^2 \rangle$	2.149	$\pm$ 0.019	$\pm$ 0.025	2.220	$\pm$ 0.069	$\pm$ 0.044	2.460	$\pm$ 0.034	$\pm$ 0.041
	β	7.14	$\pm$ 0.29	$\pm$ 0.13	9.0	$\pm$ 2.2	$\pm$ 0.3	8.81	$\pm$ 0.81	$\pm$ 0.76
comb.	$\langle p_T^2 \rangle$	2.141	$\pm$ 0.009	$\pm$ 0.015	2.204	$\pm$ 0.036	$\pm$ 0.018	2.432	$\pm$ 0.015	$\pm$ 0.028
	β	7.28	$\pm$ 0.16	$\pm$ 0.13	9.3	$\pm$ 1.3	$\pm$ 0.3	8.13	$\pm$ 0.30	$\pm$ 0.28
$\mu^+\mu^-$	w_{x_F}	0.1464	$\pm$ 0.0026	$\pm$ 0.0023	0.1453	$\pm$ 0.0088	$\pm$ 0.0051	0.1592	$\pm$ 0.0037	$\pm$ 0.0018
	Δx_F	-0.0030	$\pm$ 0.0020	$\pm$ 0.0017	-0.0076	$\pm$ 0.0056	$\pm$ 0.0021	-0.0095	$\pm$ 0.0027	$\pm$ 0.0010
	γ	1.699	$\pm$ 0.039	$\pm$ 0.014	1.45	$\pm$ 0.15	$\pm$ 0.02	1.810	$\pm$ 0.071	$\pm$ 0.016
e^+e^-	w_{x_F}	0.1482	$\pm$ 0.0042	$\pm$ 0.0014	0.149	$\pm$ 0.015	$\pm$ 0.006	0.1599	$\pm$ 0.0081	$\pm$ 0.0052
	Δx_F	-0.0016	$\pm$ 0.0029	$\pm$ 0.0034	-0.006	$\pm$ 0.010	$\pm$ 0.003	-0.0056	$\pm$ 0.0058	$\pm$ 0.0017
	γ	1.749	$\pm$ 0.075	$\pm$ 0.031	1.54	$\pm$ 0.30	$\pm$ 0.02	1.80	$\pm$ 0.17	$\pm$ 0.11
comb.	w_{x_F}	0.1468	$\pm$ 0.0022	$\pm$ 0.0016	0.1482	$\pm$ 0.0079	$\pm$ 0.0028	0.1588	$\pm$ 0.0033	$\pm$ 0.0019
	Δx_F	-0.0024	$\pm$ 0.0016	$\pm$ 0.0022	-0.0052	$\pm$ 0.0051	$\pm$ 0.0015	-0.0096	$\pm$ 0.0024	$\pm$ 0.0012
	γ	1.723	$\pm$ 0.036	$\pm$ 0.011	1.48	$\pm$ 0.14	$\pm$ 0.01	1.820	$\pm$ 0.063	$\pm$ 0.018

butions (only the statistical uncertainties are taken into account).

Also included in Table 4 are the results obtained separately in the dimuon and dielectron channels with the respective systematic uncertainties. The good agreement between the results of the two analyses within the statistical uncertainties confirms that the channel-specific issues of particle identification and counting are not responsible for large systematic variations in the shapes of the distributions.

4.2 Parameterization and interpretation of kinematic distributions

Among the parameters adopted for the description of the data, the width of the p_T distribution ($\langle p_T^2 \rangle$), the position of the maximum of the x_F distribution (Δx_F) and, possibly but less significantly, its width (w_{x_F}) show a trend with the mass number A.

It is well known [30] that the average p_T^2 of particles produced in nuclear collisions increases with the mass of the target nucleus. This trend is confirmed by the HERA-B data with high significance. The "p_T-broadening" effect is commonly explained as a consequence of multiple elastic scattering of the incoming beam parton in the surrounding nucleus before the hard scattering process takes place. The measured increase of $\langle p_T^2 \rangle$ with A is shown in Fig. 7 together with the results of experiments at lower energies. The variable of the abscissa, $A^{1/3} - 1$, is approximately proportional to the radius of the target nucleus i.e. to the average path length of the parton inside the nucleus with the shift of -1 such that the magnitude of the effect is measured with respect to $A = 1$. All measurements are actually consistent with the parameterization

$$\langle p_T^2 \rangle = \langle p_T^2 \rangle^{pp} + \rho \; (A^{1/3} - 1), \qquad (4)$$

to which they are fitted in the plot. As summarized in Fig. 8(a), the results for the average p_T^2 extrapolated to proton-nucleon interactions ($\langle p_T^2 \rangle^{pp}$) are compatible with a linear growth with the square of the center-of-mass production energy s. On the other hand, ρ is approximately independent of center-of-mass energy as can be seen in Fig. 8(b).

Furthermore, HERA-B observes a difference in shape between the x_F distributions of the J/ψ for different target nuclei consisting of an increasing displacement of the center of the distribution towards negative values. As shown in Fig. 9, J/ψs are produced in tungsten with an x_F distribution which has equal or slightly greater width with respect to those produced in carbon and tends to be asymmetrically centered at a lower value. This behavior is also supported by a fit of the E789 gold data [3] ($-0.035 < x_F < 0.135$, $E_b = 800\,\mathrm{GeV}$) with Eq. 3. The fitted width of 0.11 ± 0.01 is lower than our value for tungsten suggesting not only that the maximum is shifted but that the shape becomes asymmetric. As a possible interpretation, the effect may be attributed to the energy loss undergone by the incident parton and/or the produced state in their path through the nucleus, causing a reduction of the average x_F of the J/ψ and a possible additional smearing of the momentum distribution. This hypothesis motivates the choice of representing the data also in this case as a function of $A^{1/3} - 1$. The points in Fig. 9 (a) and b) are fitted respectively with:

$$w_{x_F} = w_{x_F}^{pp} + \tau \; (A^{1/3} - 1), \qquad (5)$$

$$\Delta x_F = \kappa \; (A^{1/3} - 1), \qquad (6)$$

where κ, $w_{x_F}^{pp}$ and τ are free parameters.

To obtain the best description of the dependence of the p_T and x_F spectra on the target nucleus, a simultaneous fit of the three (C, Ti and W) distributions according to the
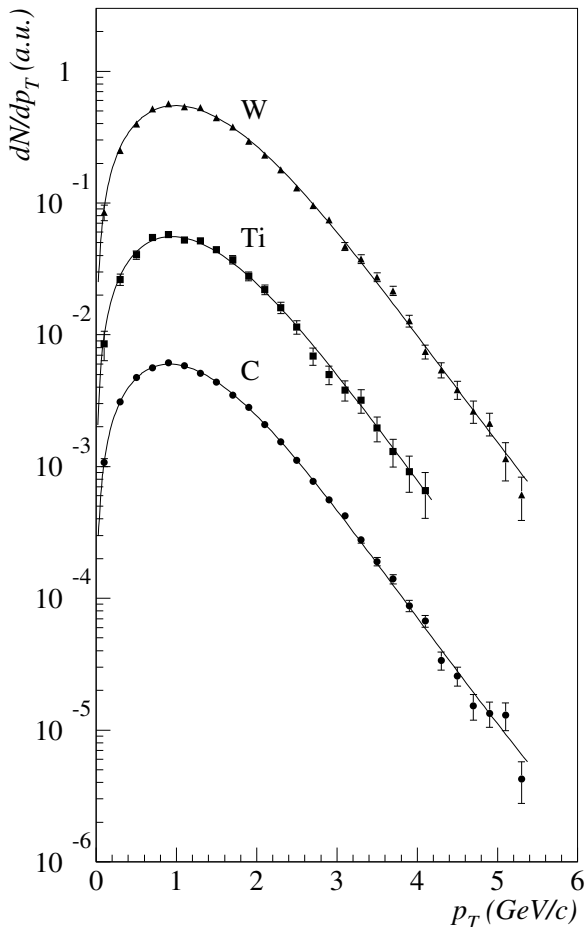
Fig. 4. Inclusive p_T distributions of J/ψ mesons for three target materials with arbitrary normalizations. For visibility, the scales are shifted arbitrarily. The error bars represent the combination of statistical and systematic uncertainties. The interpolating lines are the results of a simultaneous fit of the three p_T distributions to Eq. 2 performed with the method described in Sec. 4.2.
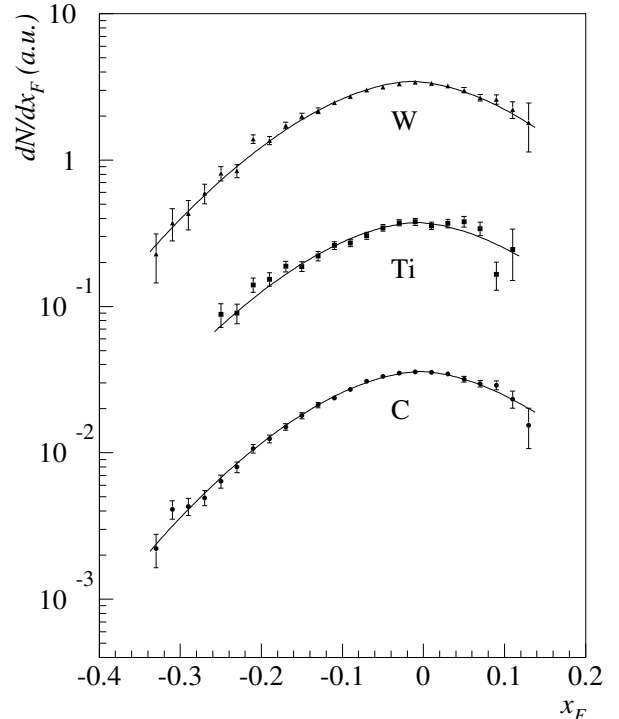

Fig. 5. Inclusive x_F distributions of J/ψ mesons for the three target materials with arbitrary normalizations. For visibility, the scales are shifted arbitrarily. The error bars represent the combination of statistical and systematic uncertainties. The interpolating lines are the results of a simultaneous fit of the three x_F distributions to Eq. 3 performed with the method described in Sec. 4.2.
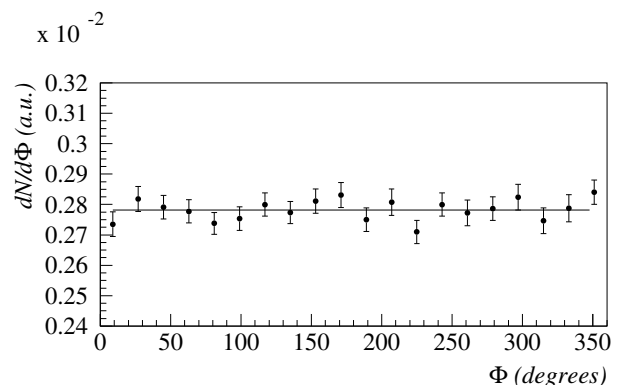

Fig. 6. Distribution of the azimuthal production angle of the J/ψs fitted to a constant. The error bars include only statistical contributions.

functions given in Eq. 2 and 3 has been done. According to the hypothesis that energy loss is responsible for the observed nuclear dependence of the shape of the kinematic distributions, the fit has been constrained by imposing the relations from Eqs. 4, 5 and 6, and, moreover,

$$\beta = \beta^{pp} + \beta'(A^{1/3} - 1), \qquad (7)$$

$$\gamma = \gamma^{pp} \text{ (independent of } A), \qquad (8)$$

where β^{pp}, β' and γ^{pp} are additional parameters of the fit. In Table 5 the results of this procedure are summarized. The fit of the x_F distributions has been performed in two variants, with the parameter τ left free or fixed to zero – therefore assuming in the latter case that w_{x_F} is independent of A. The resulting best-fit curves are the interpolating lines plotted in Figs. 4 and 5 (with $\tau = 0$). The fit results indicate a significant nuclear dependence not only of the p_T distribution (parameter ρ), but also of the x_F distribution: there is a significance of 7σ for $\kappa \neq 0$
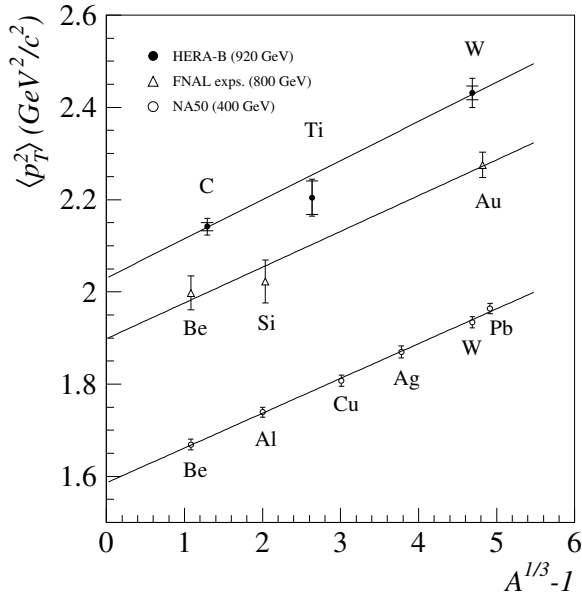
Fig. 7. The $\langle p_T^2 \rangle$ of the produced J/ψs as a function of $A^{1/3}-1$ (see Eq. 4). The results of the present analysis (black filled circles with total and statistical uncertainties) are compared to previous measurements performed with different beam energies at Fermilab [3] and at the SPS [5]. The data are fitted with linear functions.

Table 5. Results of the global fits of p_T and x_F distributions described in the text. The first of the given uncertainty ranges is statistical and the second is systematic. The following couples of parameters are significantly correlated: β^{pp} and β' (-70%), $|\kappa|$ and τ (-60%), $w_{x_F}^{pp}$ and τ (-50%), $w_{x_F}^{pp}$ and γ^{pp} (50%).

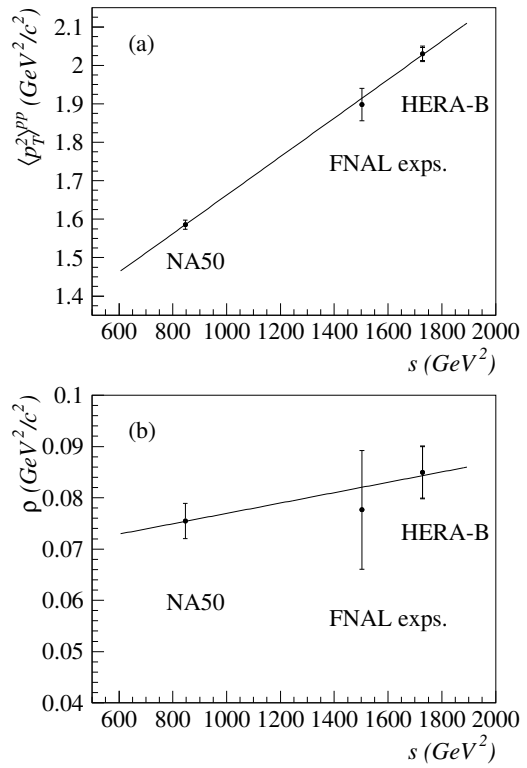| p_T distribution			
$\langle p_T^2 \rangle^{pp}$ (GeV^2/c^2)	2.030	$\pm$ 0.014	$\pm$ 0.014
ρ (GeV^2/c^2)	0.085	$\pm$ 0.005	$\pm$ 0.004
β^{pp}	6.97	$\pm$ 0.22	$\pm$ 0.23
β'	0.261	$\pm$ 0.087	$\pm$ 0.07
$\chi^2/NDoF$	106.5/71		
x_F distribution, τ free			
κ	-0.0021	$\pm$ 0.0004	$\pm$ 0.0002
$w_{x_F}^{pp}$	0.1435	$\pm$ 0.0017	$\pm$ 0.0046
τ	0.0028	$\pm$ 0.0007	$\pm$ 0.0009
γ^{pp}	1.735	$\pm$ 0.029	$\pm$ 0.014
$\chi^2/NDoF$	72/60		
x_F distribution, $\tau = 0$			
κ	-0.00295	$\pm$ 0.00035	$\pm$ 0.00018
$w_{x_F}^{pp}$	0.1478	$\pm$ 0.0014	$\pm$ 0.0028
τ	0 (fixed)		
γ^{pp}	1.725	$\pm$ 0.003	$\pm$ 0.002
$\chi^2/NDoF$	91.5/61		

Fig. 8. Energy dependence of the parameters $\langle p_T^2 \rangle^{pp}$ (a) and ρ (b) as defined in Eq. 4 describing the p_T-broadening of the J/ψ. The points represent the results obtained by HERA-B (black filled circles, with total and statistical uncertainties), at Fermilab [3] and at the SPS [5]. The data are fitted with linear functions.

when τ is fixed to zero, which changes to 4 and 3σ, respectively, for κ and τ (with a strong anti-correlation between the two) when both are left free.

5 Nuclear dependence of J/ψ production

The Glauber Model [31] suggests that the dependence of the J/ψ production cross section on atomic mass number (A) can be approximated by a power law:

$$\sigma_{pA} = \sigma_{pN} \cdot A^\alpha , \qquad (9)$$

where σ_{pN} is the proton-nucleon cross section and α, the "suppression" parameter, characterizes the nuclear dependence. Pure hard scattering in the absence of any nuclear effects would correspond to α equal to unity. A suppression of J/ψ production would lead to $\alpha < 1$ while an enhancement (anti-screening effect) would be signaled by $\alpha > 1$. Usually, α is described and measured as a function of x_F and p_T (see for example [4,5,32]).

Eq. 9 is generally used to describe data and predictions independently of particular mechanisms of nuclear modification. In general, however, α may depend on A and thus depend on the targets used to make the measurement. For
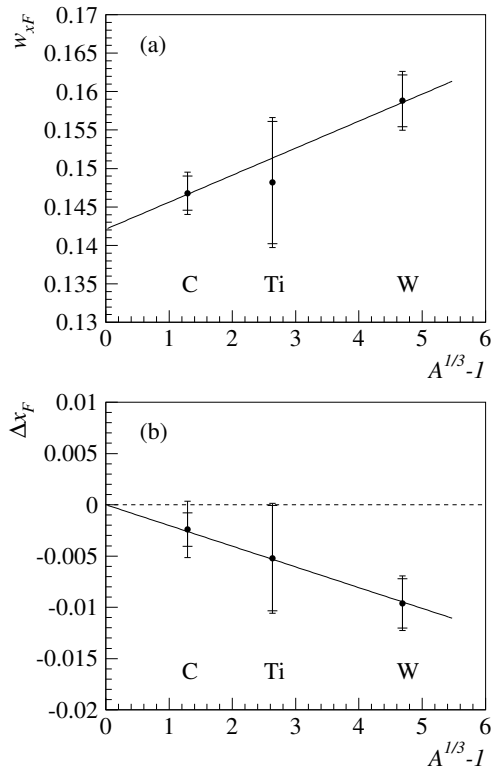
Fig. 9. The width (a) and shift (b) of the J/ψ x_F distributions as a function of $A^{1/3} - 1$ (see Eqs. 5 and 6). The double error bars represent total and statistical uncertainties. The data are fitted with linear functions.

the measurement presented here, α is evaluated by comparing the J/ψ yields from two different targets: carbon and tungsten[3] as a function of x_F and p_T.

5.1 The α measurement

Using Eq. 9, the nuclear suppression parameter α can be extracted from a measurement of the ratio of cross-sections for carbon (C) and tungsten (W) targets:

$$\frac{\sigma_{pW}}{\sigma_{pC}} = \left(\frac{A_W}{A_C} \right)^\alpha . \tag{10}$$

The measurement of the cross section ratio requires a measurement of the ratio of the integrated luminosities of the carbon and tungsten target samples. For the HERA-B setup, this can be done using data samples where two different targets are operated simultaneously (double-target runs) since most of the systematic uncertainties cancel and an absolute luminosity measurement can be avoided. On the other hand, for studies of the dependence of α on the

---

[3] The titanium sample is not used for this analysis since it is too small to have a significant impact on the statistical precision of the result and would have required a significantly more complex analysis procedure.

kinematic variables, greater statistical precision can be obtained by also using the single-target runs. The HERA-B measurement of α thus consists of two sub-measurements: a measurement of the average value of α, $\langle \alpha \rangle$, over the full visible kinematic range and a measurement of $\alpha - \langle \alpha \rangle$ as a function of x_F and p_T. The shape distributions are then corrected using $\langle \alpha \rangle$ to produce an absolute measurement of the distribution of α over the measured range.

More specifically, $\langle \alpha \rangle$ is evaluated using double target runs based on the formula:

$$\langle \alpha \rangle = \frac{\ln(\frac{\sigma_W}{\sigma_C})}{\ln(\frac{A_W}{A_C})} = \frac{1}{\ln(\frac{A_W}{A_C})} \cdot \ln \left(\frac{N_W}{N_C} \cdot \frac{\mathcal{L}_C}{\mathcal{L}_W} \cdot \frac{\epsilon_C}{\epsilon_W} \right) , \tag{11}$$

where N_X (X=C,W) denotes the total number of reconstructed J/ψ mesons originating from the corresponding target wire, $\mathcal{L}_X$ is the luminosity, ϵ_X is the overall detection efficiency (see Sec. 2). The event yields are derived as discussed in Sec. 3. The measurement of the luminosity ratios is described in Sec. 5.2.

The dependence of α on x_F and p_T is obtained from the full carbon and tungsten target data samples (double- and single-target runs). The full carbon sample is roughly twice the size of the double-target subsample while the full tungsten sample is 10% larger than the double-target subsample. The shape of the differential distributions are given by (here written e.g. for x_F):

$$\frac{1}{\sigma_{J/\psi}} \cdot \frac{d\sigma_{J/\psi}}{d x_F} , \tag{12}$$

where $\sigma_{J/\psi} = \sigma(pA \to J/\psi + X)$ is the total visible J/ψ cross section.

The measurement of nuclear effects can then be derived from the distributions of Eq. 12 using (here written e. g. for x_F):

$$\alpha(x_F) = \frac{1}{\ln \left(\frac{A_W}{A_C} \right)} \cdot \ln \left(\frac{\frac{1}{\sigma_W} \cdot \frac{d\sigma_W}{d x_F}}{\frac{1}{\sigma_C} \cdot \frac{d\sigma_C}{d x_F}} \right) + \langle \alpha \rangle . \tag{13}$$

5.2 Luminosity ratios

The luminosity acquired on target X, where X is either C (carbon) or W (tungsten), can be expressed as:

$$\mathcal{L}_X = \frac{N_X}{\sigma_X^{\text{inel}}} = \frac{\lambda_X \cdot N^{BX}}{\sigma_X^{\text{inel}}} , \tag{14}$$

where N_X is the total number of inelastic interactions occurring on target X during the measurement, σ_X^{inel} is the total inelastic cross section, N^{BX} is the corresponding total number of filled bunch crossings (BX) and λ_X is the average number of interactions per filled BX. The total cross sections σ_X^{inel} for each target material together with some details on this topic can be found in [33]. The luminosity ratio $R_{\mathcal{L}}$ needed in Eq. 11 is then given by:

$$R_{\mathcal{L}} = \frac{\mathcal{L}_C}{\mathcal{L}_W} = \frac{\sigma_W^{\text{inel}}}{\sigma_C^{\text{inel}}} \cdot \frac{\lambda_C}{\lambda_W} . \tag{15}$$

Assuming the interaction probability on target X follows a Poisson distribution, λ_X can be calculated from the observed number of events with at least one interaction $(N(\geq 1)^{\mathrm{obs}})$ using:

$$\lambda_X = \frac{1}{\epsilon_X^{inel}} \ln\left(1 - \frac{N(\geq 1)^{\mathrm{obs}}}{N^{\mathrm{BX}}}\right), \qquad (16)$$

where ϵ_X^{inel} is the probability to observe a single interaction.

The determination of λ_X relies on random-trigger events which were accumulated together with the dilepton-trigger events used for J/ψ counting. Five methods which differ by the event characteristics used to define the presence of an interaction are used to count events. All methods rely on tracks found in the vertex detector. To maintain high efficiency, the requirements imposed are minimal but sufficient to also keep the probability of incorrect target wire assignment at a low level. The methods are based on the following five criteria:

For all events,
1. ≥ 1 primary vertex on wire X where the primary vertex is formed from tracks measured both in the VDS and OTR ("long tracks"),
2. ≥ 2 tracks (including long tracks and tracks seen only in the VDS) with impact parameter $\leq 3\sigma$ of wire X and $\geq 5\sigma$ from the other wire, where σ is the impact parameter measurement uncertainty,

and, using the subset of events with no vertex found on the other wire,

3. ≥ 1 primary vertex on wire X using all tracks,
4. ≥ 1 primary vertex on wire X using long tracks only,
5. ≥ 2 long tracks within $\leq 3\sigma$ from wire X.

Both as a cross check and as an estimate of the systematic uncertainty on the efficiency, all counting methods are checked in parallel. For the final luminosity ratio determination, the average of the five determinations is used and the rms spread of the five is factored into the systematic uncertainty. (The alternative uncertainty calculation using the maximum variation of results divided by $\sqrt{12}$ which appears elsewhere in this paper produces somewhat smaller uncertainties. To be conservative, we choose the larger estimate.) Furthermore, Eq. 16 assumes that the interaction probabilities for each wire follow a Poisson distribution. However, the individual bunch fillings are often uneven and the interaction rate varies in time by typically 20%. To quantify this influence, an alternative luminosity calculation is performed in which the detailed bunch filling structure and the interaction rate distribution on each wire are taken into account. The differences between the resulting ratios and those computed directly from Eq. 15 are negligible compared to other systematic uncertainties.

To minimize the dependence of the efficiency estimate on MC, the efficiency of each of the above methods is calibrated by comparing the luminosity estimate found using it with that found by the methods described in [33]. These latter methods rely on very simple criteria to identify events with interactions, such as a minimal number of hits in the RICH detector (typically twenty, compared to thirty hits expected for a fully accepted fast charged particle) or a small (1 GeV) energy deposit in the ECAL and are estimated to be sensitive to roughly 95% of the total non-diffractive cross section.

Each target of a two-wire configuration is calibrated separately using single-wire data runs taken nearby in time to the run being calibrated. A "ghost" wire is introduced at the location of the other wire of the configuration. Thus the MC is not relied on to model tracking in the VDS or vertex finding, but only to estimate the efficiency of simpler and more robust event counting techniques described in [33]. Overall efficiencies in the range of $60-80$ % are found, depending on method and wire. The efficiency-calibration method based on real data is also used to evaluate the probability that interactions are assigned to the wrong wire. This probability is method and configuration dependent and is never more than 0.4%.

The average relative systematic uncertainties on the luminosity ratios due to interaction counting and MC calibration [33] are 1.3% and 3.2%, respectively, giving an overall scale uncertainty of 3.4% on $R_{\mathcal{L}}$. Depending on wire configuration between 0.6 and 1.2 million events were used for the determination of λ_{C} and λ_{W}, thus the statistical uncertainty on the luminosity ratio is negligible.

5.3 Results

Based on Eq. 11, an average suppression value of

$$\langle\alpha\rangle = 0.981 \pm 0.004_{\mathrm{stat.}} \pm 0.016_{\mathrm{sys.}} \qquad (17)$$

in the visible range of x_F is obtained. As explained in Sect. 2, the target system of HERA-B consisted of eight different wires grouped in two stations. The data were taken with four different two-wire configurations which were analyzed separately and averaged to obtain the final value. Also, the electron and the muon decay channels represent two statistically independent measurements. The average value is calculated as a weighted mean with weights being the squared quadratic sum of statistical and luminosity ratio uncertainties. The luminosity ratios are determined for each wire configuration separately as discussed in Sec. 5.2 with a contribution to the systematic uncertainty on $\langle\alpha\rangle$ of $3.4\,\%/\ln(A_W/A_C) = 1.24\,\%$. A systematic effect of 1.1% due to time variatons of detector performance and imprecisions in detector or trigger simulations was estimated from the variations of $\langle\alpha\rangle$ among the four samples and two decay channels. The total systematic uncertainty on $\langle\alpha\rangle$ is thus 1.66 %. The statistical precision of the $\langle\alpha\rangle$ measurement contributes an uncorrelated uncertainty 0.4 %.

The values of α for individual x_F and p_T bins are given in Table 6 and shown in Fig. 10 for p_T and in Fig. 11 for x_F. They will be further discussed in Sec. 5.4. The values and systematic uncertainty estimates were derived according to the procedure described in Sec. 4.1. The error bars on the figures show both statistical and total contributions. The systematic uncertainties in the estimate of $\langle\alpha\rangle$
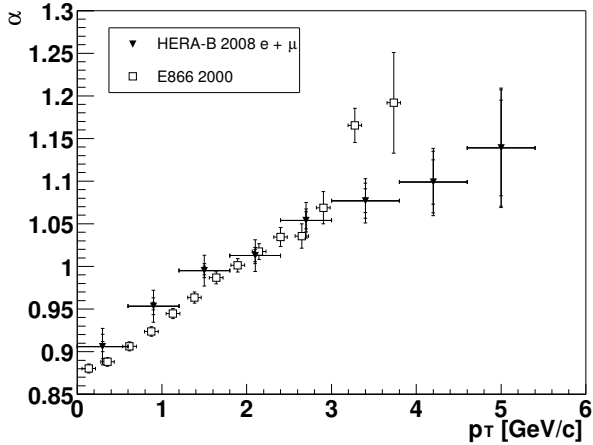
Fig. 10. The nuclear suppression parameter α as a function of p_T measured by HERA-B (filled triangles, plotted with total and statistical uncertainties) and by E866 [4] (empty squares).

are largely uncorrelated with those from the $\alpha - \langle \alpha \rangle$ measurement. The final systematic uncertainty estimate is the quadratic sum of the two. The systematic uncertainty is substantially correlated from bin to bin.

5.4 Discussion

The results of the α measurement as functions of p_T and x_F are given in Table 6. The distributions of the $\alpha(p_T)$ and $\alpha(x_F)$ are presented in Figs. 10 and 11 where they are compared with measurements performed by other fixed target experiments: E866 [4] ($E_p = 800\,\mathrm{GeV}$) and NA50 [5] ($E_p = 450\,\mathrm{GeV}$). As already seen (e.g. in Fig. 7), the measured p_T dependence of the nuclear modification effects is very similar for HERA-B and E866. In Fig. 11 the E866 and HERA-B measurements are seen to be compatible within statistical and systematic uncertainties in the overlap region. The NA50 results are based on lower energy collisions and are systematically below both HERA-B and E866. At lower values of x_F, the HERA-B $\alpha(x_F)$ measurement indicates a reversal of the suppression trend seen at high x_F: the strong suppression established by previous measurements at high x_F turns into a slight tendency towards enhancement in the negative x_F region.

The dependence of J/ψ production in hadron-nucleus interactions on x_F has been modeled by Vogt [6,7]. Nuclear effects caused by final-state absorption, interactions with co-movers, shadowing of parton distributions, energy loss and intrinsic charm quark components are described separately and integrated into the model. It is further assumed that the $c\bar{c}$ pair is subject to more severe energy losses if produced in a color octet state. Four curves from this model which differ in their descriptions of nuclear Parton Density Functions (nPDF) and energy loss are shown in Fig. 11. All calculations shown here were done for the center-of-mass energy of HERA-B at $\sqrt{s} = 41.6\,\mathrm{GeV}$. The nPDF distributions of Eskola, Kolhinen and Salgado (EKS) [34] describe the scale dependence of the ratios of

Table 6. The parameter α as a function of p_T and x_F. Statistical and systematic uncertainties are indicated separately. They were extracted from the measurement using Eqs. 13 and 17.

p_T (GeV/c) min	max	α
0.0	0.6	$0.906 \pm 0.006 \pm 0.021$
0.6	1.2	$0.953 \pm 0.005 \pm 0.019$
1.2	1.8	$0.995 \pm 0.005 \pm 0.017$
1.8	2.4	$1.013 \pm 0.007 \pm 0.018$
2.4	3.0	$1.054 \pm 0.010 \pm 0.019$
3.0	3.8	$1.077 \pm 0.014 \pm 0.021$
3.8	4.6	$1.099 \pm 0.026 \pm 0.028$
4.6	5.4	$1.139 \pm 0.056 \pm 0.038$

x_F min	max	α
-0.34	-0.26	$1.036 \pm 0.034 \pm 0.042$
-0.26	-0.22	$1.012 \pm 0.023 \pm 0.030$
-0.22	-0.18	$1.031 \pm 0.014 \pm 0.023$
-0.18	-0.14	$1.015 \pm 0.010 \pm 0.020$
-0.14	-0.10	$0.994 \pm 0.008 \pm 0.018$
-0.10	-0.06	$0.978 \pm 0.006 \pm 0.018$
-0.06	-0.02	$0.967 \pm 0.005 \pm 0.017$
-0.02	0.02	$0.967 \pm 0.006 \pm 0.018$
0.02	0.06	$0.962 \pm 0.008 \pm 0.021$
0.06	0.14	$0.947 \pm 0.015 \pm 0.028$

nPDFs of a proton inside a nucleus to those of a free proton within the framework of lowest order leading-twist DGLAP evolution [35] by evolving the initial PDF from the CTEQ4L [36] and leading order GRV [37] parameterizations. An improved leading-order DGLAP analysis of nPDFs including next to leading order calculations has been published recently by Eskola, Paukkunen and Salgado (EPS) [38]. In another approach by Hirai, Kumano and Nagai (HKN) [39], nuclear structure function ratios $F_2^A/F_2^{A'}$ and Drell-Yan cross section ratios are analyzed to obtain nPDFs. The HKN analysis shows weak anti-shadowing at negative x_F.

Initial state energy loss as described by Gavin and Milana (GM) [9] and modified by Brodsky and Hoyer (BH) [10] is based on a multiple scattering approach that essentially depletes the projectile parton momentum fraction as the parton moves through the nucleus. Both quarks and gluons can scatter elastically and therefore lose energy prior to the hard process resulting in an effective reduction of J/ψ production for $x_F > 0$.

The measurement of HERA-B shows that α increases with decreasing x_F and suggests enhanced J/ψ production for $x_F < -0.1$. The HERA-B data favors the nPDFs of EPS and HKN over EKS. The BH description of energy loss is clearly ruled out. None of the variants of the Vogt model give a satisfactory description of both HERA-B and E866 data. For example, while the HKN curve is compatible with most of the HERA-B data points at negative x_F,
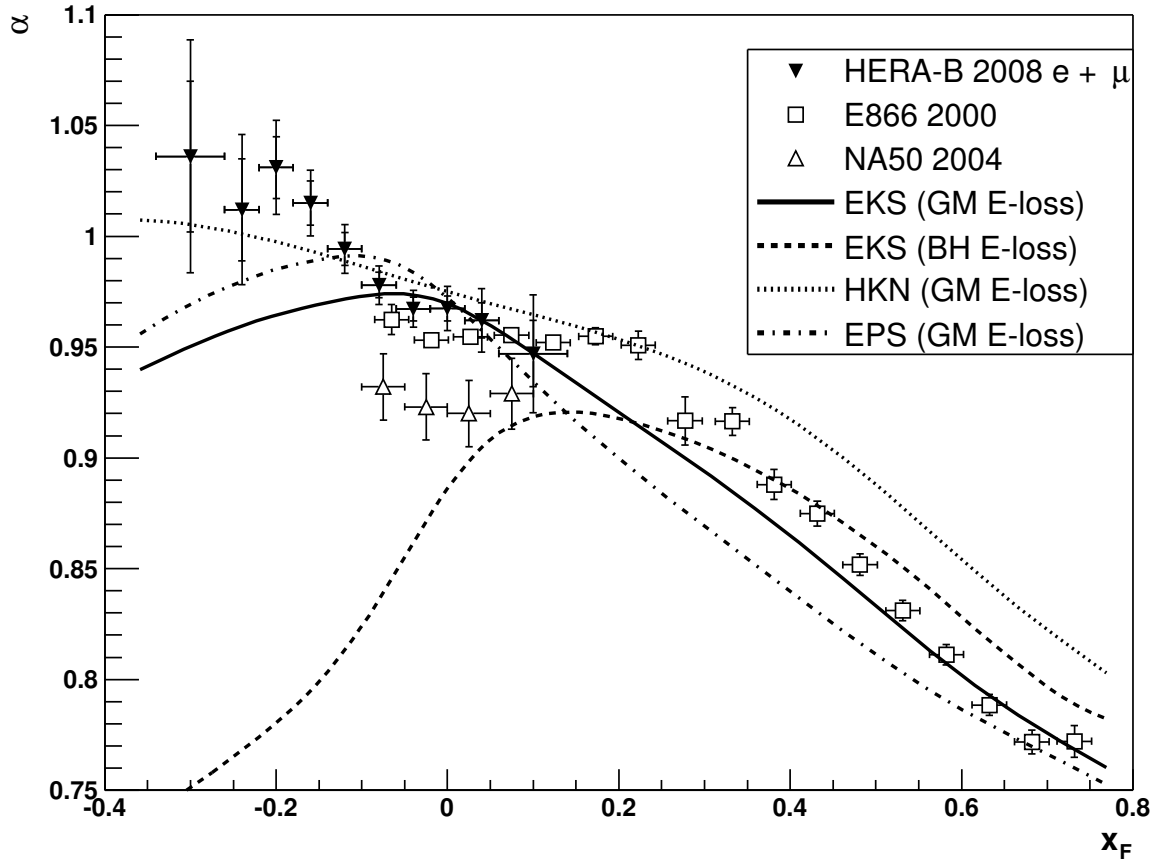
16

Fig. 11. Measurements of α as a function of x_F by HERA-B (filled triangles, plotted with total and statistical uncertainties), E866 ($\sqrt{s} = 38.8\,\mathrm{GeV}$) [4] (empty squares) and NA50 ($\sqrt{s} = 29.0\,\mathrm{GeV}$) [5] (empty triangles). The curves were calculated by Vogt [6,7] based on three different nuclear parton distribution functions: (EPS [38], EKS [34,40] and HKN [39]) and two models of initial state energy-loss: BH [9] and GM [9]. For all approaches, energy loss, intrinsic charm and shadowing are taken into account.

it lies significantly above the E866 points and furthermore fails to adequately describe RHIC data [38].

Another theoretical model by Boreskov and Kaidalov [8], formulated in the framework of reggeon phenomenology, predicts an anti-screening effect in the region of negative x_F. An important ingredient of their model is the assumption that a colorless state containing c and $\bar{c}$ quarks which has some probability of projecting into a charmonium state is produced and propagates through the nucleus. The colorless state is of large size, possibly consisting of $D\bar{D}$ or $D^*\bar{D}^*$ mesons, and therefore has a large interaction cross section. As it propagates through the nucleus it interacts and loses energy. Ultimately, the observed J/ψ mesons are projected out of the energy-depleted colorless state. The measurements of HERA-B are qualitatively compatible with the calculations described in BK [8].

6 Conclusions

HERA-B has performed the first determination of the nuclear dependence of J/ψ production kinematics at neg-

ative x_F in proton-nucleus collisions. The analyzed data samples were obtained in collisions of protons from the 920 GeV HERA-proton beam with carbon, tungsten and titanium targets. The J/ψ mesons are observed in both dimuon and dielectron decay channels. The comparison of results from the two channels affords some additional control over systematic uncertainties arising from triggering and selection procedures.

The measurement covers the kinematic range $-0.34 < x_F < 0.14$ and $p_T < 5.4\,\mathrm{GeV/c}$. The measured dN/dp_T distribution is seen to become broader with increasing atomic mass number as has already been observed by experiments at lower center-of-mass energies [3,5]. The data indicates that the dN/dx_F distribution also tends to become broader and that its center moves towards negative x_F values with increasing A.

The dependences of the nuclear suppression parameter, α, on p_T and x_F are also presented. The α parameter is seen to increase with increasing p_T in agreement with data from E866 [4]. In the x_F region of overlap of the two experiments, the two α measurements are mutually consistent. As x_F decreases, α increases and becomes greater than 1 below $x_F \approx -0.15$, although the data remains com-

patible with a value of 1 to within 2σ. Thus instead of the strong suppression observed at high positive x_F, HERA-B measured no suppression or a possible enhancement of J/ψ production at negative x_F. Hard-scattering based models [6,7] have difficulty simultaneously accommodating the HERA-B, E866 and RHIC measurements, while the reggeon-inspired model of Boreskov and Kaidalov [8] is in qualitative agreement with the HERA-B and E866 data.

Acknowledgments

References

1. I. Abt *et al.* (HERA-B Collaboration), Eur. Phys. J. **C49** (2007) 545.
2. I. Abt *et al.* (HERA-B Collaboration), Phys. Rev. **D79** (2009) 012001.
3. M. Kowitt *et al.* (E789 Collaboration), Phys. Rev. Lett. **72** (1994) 1318;
   M.H. Schub *et al.* (E789 Collaboration), Phys. Rev. **D52** (1995) 1307;
   T. Alexopoulos *et al.* (E771 Collaboration), Phys. Rev. **D55** (1997) 3927;
   L. Gribushin *et al.* (E672/706 Collaboration), Phys. Rev. **D62** (2001) 012001-1.
4. M.J. Leitch *et al.*, Phys. Rev. Lett. **84** (2000) 3256.
5. B. Alessandro *et al.* (NA50 Collaboration), Eur. Phys. J. **C33** (2004) 31;
   C. Lourenço, Nucl. Phys. **A783** (2007) 451.
6. R. Vogt, Phys. Rev. **C61** (2000) 035203.
7. R. Vogt, Phys. Rev. **C71** (2005) 054902.
8. K.G. Boreskov and A.B. Kaidalov, JETP Lett. **D77** (2003) 599.
9. S. Gavin and J. Milana, Phys. Rev. Lett. **68** (1992) 1834.
10. S. Brodsky and P. Hoyer, Phys. Lett. **B298** (1993) 165.
11. S. Zakharov, Phys. Atom. Nucl. **B61** (1998) 838.
12. D. Kharzeev and H. Satz, Z. Phys. **C60** (11993) 389.
13. E. Hartouni *et al.*, HERA-B Design Report, DESY-PRC-95-01 (1995).
14. K. Ehret *et al.* (for the HERA-B Collaboration), Nucl. Instr. Methods **A446** (2000) 190.
15. C. Bauer *et al.* (for the HERA-B Collaboration), Nucl. Instr. Methods **A453** (2000) 103.
16. T. Zeuner, (for the HERA-B Collaboration), Nucl. Instr. Methods **A446** (2000) 324;
   Y. Bagaturia, Nucl. Instr. Methods **A490** (2002) 223.
17. H. Albrecht *et al.* (for the HERA-B Collaboration), Nucl. Instr. Methods **A576** (2007) 312.
18. J. Pyrlik, Nucl. Instr. Methods **A446** (2000) 299; I. Ariño *et al.* (for the HERA-B Collaboration), Nucl. Instr. Methods **A453** (2000) 289.
19. G. Avoni *et al.*, Nucl. Instr. Methods **A580** (2007) 1209; A. Zoccoli *et al.* (for the HERA-B Collaboration), Nucl. Instr. Methods **A446** (2000) 246.
20. M. Buchler *et al.* (for the HERA-B Collaboration), IEEE Trans. Nucl. Sci. **NS-46** (1999) 126;
   A. Arefiev *et al.*, IEEE Trans. Nucl. Sci. **NS-48** (2001) 1059.
21. M. Böcker *et al.*, IEEE Trans. Nucl. Sci. **NS-48** (2001) 1270;
   Yu. Gilitsky *et al.*, Nucl. Instr. Methods **A461** (2001) 104.
22. V. Egorytchev *et al.* (for the HERA-B Collaboration), IEEE Trans. Nucl. Sci. **NS-50** (2003) 859.
23. P. Kreuzer (for the HERA-B Collaboration), Nucl. Instr. Methods **A462** (2001) 212.
24. T. Sjöstrand, Comp. Phys. Comm. **82** (1994) 74.
25. H. Pi, Comp. Phys. Comm. **71** (1992) 173.
26. R. Brun *et al.*, GEANT3, Internal Report CERN DD/EE/84-1, CERN, 1987.
27. A. Spiridonov, DESY report 04-105 (2004), hep-ex/0510076.
28. I. Abt *et al.* (HERA-B Collaboration), Phys. Lett. **B638** (2006) 407.
29. I. Abt *et al.* (HERA-B Collaboration), to be published in Eur.Phys.J.C.
30. J.W. Cronin *et al.*, Phys. Rev. **D11** (1975) 3105.
31. R.J. Glauber and M. Matthiae, Nucl. Phys. **B21** (1970) 135.
32. I. Abt *et al.* (HERA-B Collaboration), Eur. Phys. J. **C50** (2007) 315.
33. I. Abt *et al.* (HERA-B Collaboration), Nucl. Instr. Methods **A582** (2007) 401.
34. K.J. Eskola, V.J. Kolhinen and C.A. Salgado, Eur. Phys. J. **C9** (1999) 61.
35. Y. Dockshitzer, JETP **46**(1977)1946; V.N. Gribov and L.N. Lipatov, Sov.Nucl.Phys. **15**(1972)438;
   G. Altarelli and G. Parisi, Nucl. Phys. **B126** (1977) 298.
36. H.L. Lai *et al.*, Phys. Rev. **D55** (1997) 1280.
37. M. Glück, E. Reya and A. Vogt, Z. Phys. **C53** (11992) 127.
38. K. J. Eskola, H. Paukkunen and C. A. Salgado, arXiv:0802.0139 [hep-ph].
39. M. Hirai, S. Kumano and T. H. Nagai, Phys. Rev. **C70** (2004) 044905.
40. K. J. Eskola, V. J. Kolhinen and P. V. Ruuskanen, Nucl. Phys. **B535** (1998) 351.